OPEN ACCESS
IOP Publishing | International Atomic Energy Agency Nuclear Fusion
Nucl. Fusion **62** (2022) 026020 (12pp) https://doi.org/10.1088/1741-4326/ac3f49

Comparison of the influence of 2D and 3D geometry of the main chamber on plasma parameters in the SOL of ASDEX Upgrade

L. Bock[1,2,*], D. Brida[2], M. Faitsch[2], K. Schmid[2], T. Lunt[2] and the ASDEX Upgrade Team[a]

[1] Physik-Department E28, Technische Universität München, 85747 Garching, Germany
[2] Max-Planck-Institut für Plasmaphysik, EURATOM-Association, Boltzmannstr. 2, D-85748 Garching, Germany

E-mail: lennart.bock@ipp.mpg.de

Received 8 June 2021, revised 29 October 2021
Accepted for publication 2 December 2021
Published 23 December 2021

Abstract

In this paper the influence of toroidally asymmetric wall features on plasma solutions for ASDEX Upgrade is investigated by using the 3D scrape-off-layer simulation code EMC3-EIRENE. A comparison of simulation results in a 2D case with a toroidally symmetric first wall and divertor and a 3D case that differs from the 2D setup by including the 3D structure of the poloidal rib-limiters on the low field side of ASDEX Upgrade, highlights notable differences in the main chamber neutral particle distributions, ionisation sources and plasma flow patterns. Both neutral particle distribution and ionisation sources extend poloidally further upwards at the outer mid-plane in the 3D case and the plasma flow is globally influenced by the 3D wall features. Both simulations are conducted with identical input parameters to isolate the influence of wall geometry from other factors. By analysing the transport of neutrals from different poloidal locations it was possible to explain the observed discrepancies by different transport paths for recycled neutrals from the divertor region, only accessible in the 3D version of the wall geometry. Together with observed differences in fall-off lengths for plasma flow and electron temperature at the outer mid-plane, presented results are of key importance for interpreting global impurity migration experiments.

Keywords: ASDEX Upgrade, plasma flow pattern, 3D SOL modelling, neutral particle transport

(Some figures may appear in colour only in the online journal)

1. Introduction

Simulated plasma background solutions for tokamak plasmas generally focus on the divertor and match experimental up- and downstream profiles of n_e and T_e in a poloidal cross section [1, 2]. The applied codes (e.g. SOLPS [3]) can mostly only deal with simple 2D geometries and thus must assume toroidal symmetry.

While the divertor is essentially toroidally symmetric, the main chamber often includes features like poloidal limiters and probes that can break this symmetry. By taking toroidal asymmetries into account, fluxes to and from these localized heat-shield elements can have an influence on the plasma, particularly on the distribution of ionization sources and thus the plasma flow pattern, which are of particular interest for impurity migrations studies.

* Author to whom any correspondence should be addressed.
[a] See Meyer *et al* 2019 (https://doi.org/10.1088/1741-4326/ab18b8) for the ASDEX Upgrade Team.

Original content from this work may be used under the terms of the Creative Commons Attribution 4.0 licence. Any further distribution of this work must maintain attribution to the author(s) and the title of the work, journal citation and DOI.

 © 2021 The Author(s). Published on behalf of IAEA by IOP Publishing Ltd

This article investigates the influence of geometrical asymmetries on numerical plasma background solutions for ASDEX Upgrade (AUG) L-mode plasma discharge #32024. This discharge was dominantly electron cyclotron resonance (ECR) heated with 0.445 MW and the nitrogen seeding was modulated to achieve an average seeding rate of 2.9×10^{20}N s^{-1} [4]. A time-trace of the discharge is shown in figure 1 where temperature and density are taken from the integrated data analysis software [5]. In order to gather information on the migration of N^{15} a collector probe was positioned at the outer mid-plane protruding slightly out of the limiter shadow and hence breaking the toroidal symmetry.

The main fuelling species D was injected from two valves, one at the outer mid-plane and one in the divertor, with a distance of roughly 67.5° in toroidal direction, while the impurity N^{15} was injected from two different, opposing valves in the divertor.

The experiment was analysed in [4] through simulations with WallDYN [6], a global impurity migration code that calculates surface compositions and impurity fluxes self consistently, using a SOLPS plasma background. It was found that the simulation overestimated the N^{15} deposition at the mid-plane probe by one to two orders of magnitude. Since in [7] WallDYN well explained the N-deposition patterns, it was hypothesized in [4] that the missing treatment of the three-dimensional geometry could explain the discrepancy between experiment and modelling. To include these effects the numerical plasma background solutions in this article were calculated with the 3D edge Monte Carlo code EMC3-EIRENE [8]. Two types of simulations were performed: one with a toroidally symmetric main chamber heat-shield matching the radial apex of the poloidal rib-limiters in AUG and one with a 3D, toroidally asymmetric heat-shield with realistic rib limiter geometry and the collector probe at the outer mid-plane.

The article first explains the simulation setup and compares the simulation results upstream at the outer mid-plane and downstream at the divertor targets with experimentally obtained data in section 2. In section 3 differences between the simulation results in toroidally symmetric and toroidally asymmetric heat-shield geometry are investigated and in section 4 influences of the different plasma solutions on plasma parameter at the mid-plane collector probe are analysed. Section 5 summarizes the results and provides an outlook of potential influences on future work.

2. Simulation setup

Based on the time traces in figure 1 and further analysis of the stability of separatrix values and divertor data for density and temperature the simulation aims to reproduce the plasma background at $t = 3$ s. The experimental values are very stable from $t = 2$–4 s and the input values for separatrix density and heating power are taken from the average of the experimental data from $t = 2.95$–3.05 s. This results in a total heating power of $P_{\mathrm{heat,tot}} \approx 0.99$ MW, consisting of ECR heating power and the ohmic heating component, a total radiated power of $P_{\mathrm{heat,tot}} \approx 0.67$ MW, a separatrix density of $n_{\mathrm{e,sep}} \approx 0.74 \times 10^{19}$ m^{-3} and an electron temperature at the separatrix of $T_{\mathrm{e,sep}} \approx 57$ eV.

Based on the magnetic configuration a 3D grid was calculated with the CLISTE equilibrium code [9] covering 30° of the torus. To extend the simulation domain to 60°, two identical segments with mapping boundary conditions in toroidal direction are used. Figure 2 shows a poloidal cross-section of the grid with representations of heat-shield elements in ASDEX Upgrade.

The geometry of the heat-shield is included in two different variations: in figure 3 the outer wall consists of two limiters and the mid-plane collector probe (MEM), resembling 60° of the torus during the discharge. The MEM is protruding 2.5 cm into the plasma with its tip being at the radius of $R = 2.156$ m while the apex of the limiters are at $R = 2.181$ m at the same height of about $z = 0.31$ m. This geometry and the related plasma background is referred to as 3D simulation. The real machine geometry features a single mid-plane deposition probe and while several rib limiters are present, they are not distributed toroidally symmetric. Note that the toroidal symmetry in this geometry is only broken upstream on the low field side (LFS), while the divertor region and the high field side (HFS) heat-shield are still assumed to be toroidally symmetric.

In figure 4 both limiters and the mid-plane collector probe are substituted by a closed wall following the apex of the limiters, reducing the geometry to two dimensions. Therefore, the related plasma solution is referred to as 2D simulation.

The presented simulations focus on the scrape-off-layer (SOL) and the simulation volume is thus radially limited to $\rho \geqslant 0.98$, where ρ is the normalized poloidal plasma radius with $\rho = 0$ at the magnetic axis and $\rho = 1$ at the separatrix. Tomographic reconstructions estimates the radiated power within $\rho \leqslant 0.98$ to be about $P_{\mathrm{rad}} = 0.4$ MW, leading to an effective heating power of $P_{\mathrm{heat,eff}} \approx 0.59$ MW and leaving $P_{\mathrm{rad,eff}} \approx 0.27$ MW to be radiated by the nitrogen impurity within the simulated domain. The nitrogen impurity is seeded from all wall tiles via chemical sputtering, while the main fuelling species deuterium is seeded from the divertor.

The necessary input parameters for EMC3-EIRENE, such as heating and radiated power, separatrix density and perpendicular transport coefficients are identical in both simulations. The resulting 2D and 3D plasma backgrounds are compared at different locations in the main chamber, the divertor and at the MEM. For the 2D simulation, which does not contain the MEM geometry, the fluxes onto the MEM are calculated using the analytical formula for ion collection by probes in plasma from [10]. The so calculated fluxes are then compared to the simulated fluxes in the 3D case.

To compare the differences in the neutral dynamic the neutral source strength from different locations at the first wall is compared. These locations are indicated by curly braces in figures 3 and 4.

In EMC3-EIRENE the parallel transport follows the Braginskii approach, but perpendicular transport is assumed to be

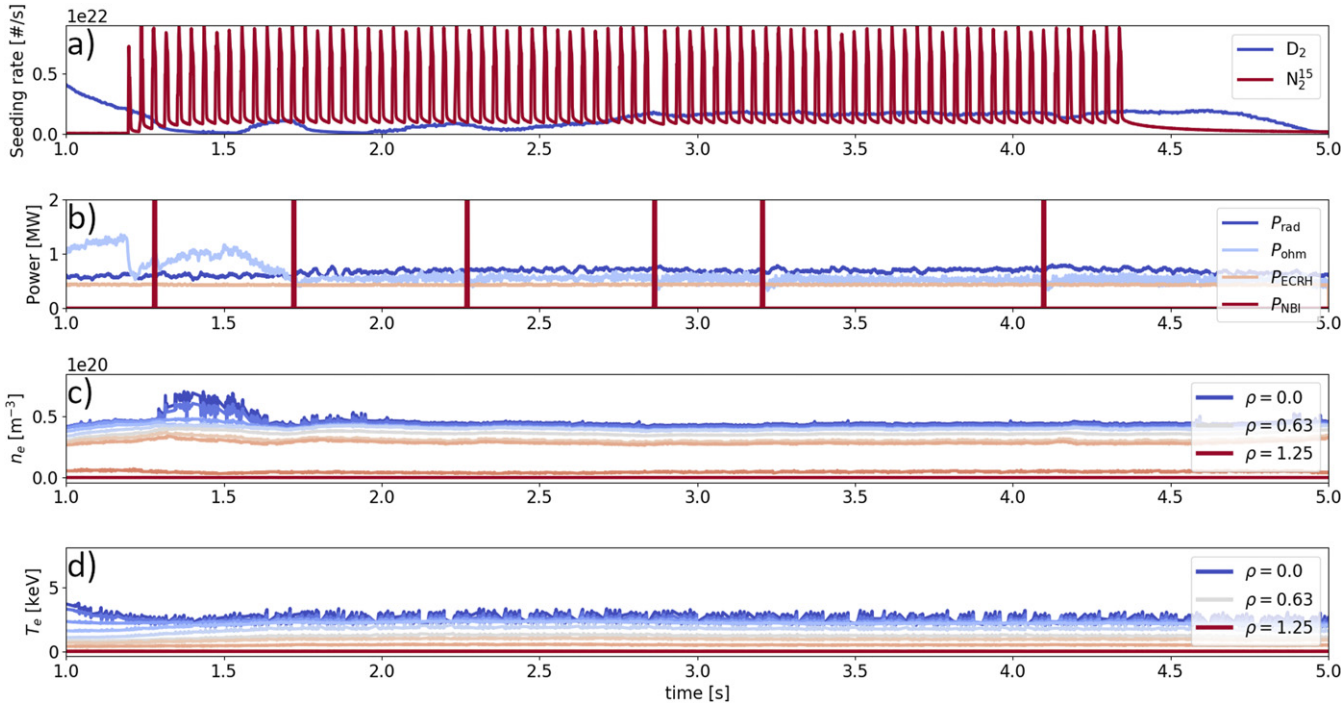

Figure 1. Time-trace of ASDEX Upgrade discharge #32024. (*a*) Deuterium and nitrogen 15 seeding rate. (*b*) ECR and Ohmic heating powers, the radiated power from the plasma and NBI blips, used to determine the ion temperature (*c*) and (*d*) electron density and temperature at different radial positions from fits to Thomson scattering and interferometer data.

anomalous following a diffusive ansatz where particle transport is described by [11]

$$\vec{\Gamma}_\perp = -D_\perp \vec{\nabla}_\perp n, \tag{1}$$

where $\vec{\Gamma}_\perp$ is the particle flux perpendicular to the magnetic field, $n = n_i = n_e$ the plasma density and $D_\perp$ the particle diffusion coefficient perpendicular to the magnetic field.

Similarly the energy transport of electrons and ions is also gradient driven and follows

$$\vec{q}_{e,i\perp} = -\chi_{e,i\perp} n \vec{\nabla}_\perp T_{e,i}, \tag{2}$$

with the heat-flux density $\vec{q}_{e,i\perp}$ of electron and ions perpendicular to the magnetic field, the perpendicular heat diffusion coefficient $\chi_{e,i\perp}$ and the temperature of electron and ions $T_{e,i}$.

In these equations, the particle diffusion coefficient $D_\perp$ and the heat diffusion coefficients $\chi_{e,i\perp}$ are the before-mentioned input parameters for the perpendicular transport. They are determined by iterative fitting of simulation results to experimental data upstream at the mid-plane and downstream at the divertor until a reasonable agreement is achieved.

The simulation volume is confined radially by the vessel wall and in the plasma core at $\rho = 0.98$. The vessel wall is treated like all targets, where impinging majority plasma ions are re-emitted as fast atoms or thermal molecules [12]. The core acts as an energy source and for impurities reaching the core boundary the surface-average flux is set to be zero for all charge states. The overall balance of particles is maintained by scaling the recycling flux such that the upstream separatrix density equals the experimentally obtained value. Additional pumping is accounted for by surface behind the outer divertor with an albedo of 0.88. The energy from the core is given by the external heating sources and is equally split between ion and electron channels while experimental values for the radiated power define the power sink. The concentration distribution of N seeded into the plasma is calculated by EMC3-EIRENE using a force balance in parallel direction and diffusive transport perpendicular to the magnetic field (see 'diffusion convection model' in [13]). The so calculated concentration distribution of N in the plasma is then scaled such that its radiated power matches the radiated power measured in the experiment. In toroidal direction periodic boundary conditions are used.

The simulated profiles are compared to experimental up- and downstream data taken at the outer mid-plane and at the divertor targets, respectively. Figure 5 shows the comparison of simulated upstream profiles with the experimentally obtained values. The upstream profile for the 3D simulation is coloured in blue with a solid line, while the 2D case is depicted in green with a dashed line. Experimental data is indicated by the red crosses and the orange triangles. The experimental electron temperature T_e is obtained from a lithium-beam- and an edge Thomson-scattering-diagnostics, which also provides data for the electron density n_e. The data from the Thomson-scattering-diagnostics are shifted by 9 mm to match a separatrix temperature of $T_e = 50$–60 eV, which corresponds to characteristic values for L-mode discharges in AUG, as calculated by a power balance [14]. Similar values were also observed in recent parameters studies [15]. The same shift was applied to the data for the electron density and the lithium data was

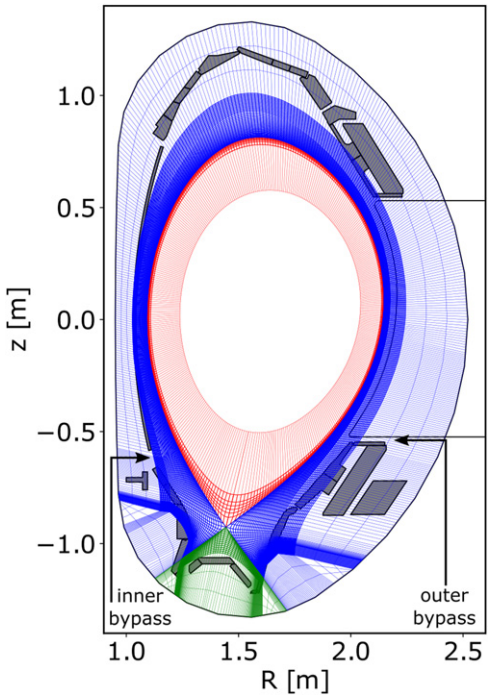

Figure 2. Poloidal cross section of the 3D grid based on the magnetic configuration of discharge #32024. The grid is structured into three zones. The private flux region is coloured in green, the SOL depicted in blue and the core shown in red. Thick lines indicate the plasma grid while the thin lines show the extended grid region for neutrals. The grey boxes represent heat-shield elements in ASDEX Upgrade with the outline of the rib limiter at the right-hand side and the outermost black line indicates the wall of the vacuum vessel. The arrows indicate the inner and outer bypass where neutral particles from behind the divertor structure can enter the plasma.

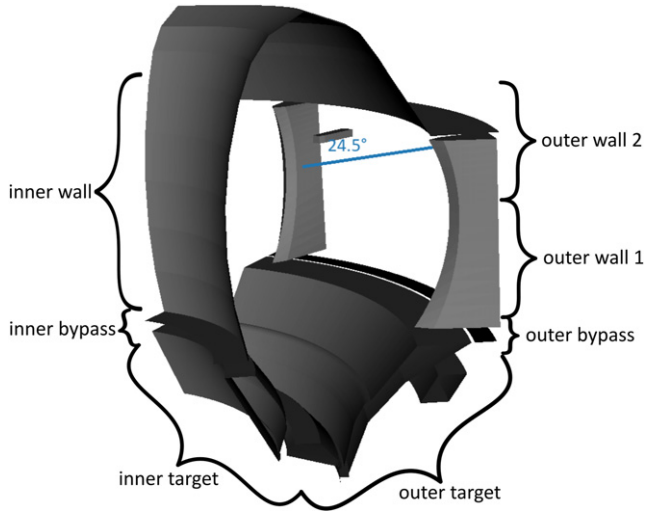

Figure 3. 60° of the 3D geometry. The blue line indicates the toroidal angle in the middle between the first limiter and the mid-plane collector probe (MEM) at $\phi = 24.5°$, where the simulation results between both geometries are presented in this article. The curly braces indicate wall areas used for recycling analysis in figure 9.

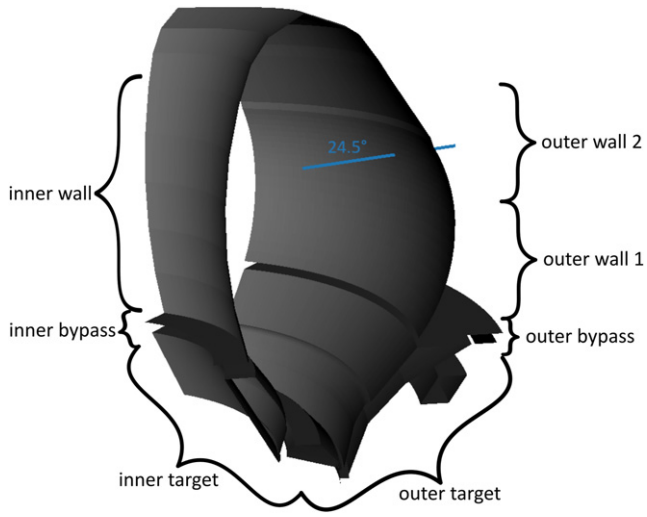

Figure 4. 60° of the 2D geometry with the blue line indicating the toroidal angle $\phi = 24.5°$ as in figure 3.

shifted by −3 mm to match the Thomson data at the separatrix. This is a standard procedure used on AUG for the edge profiles, as both the magnetic equilibrium reconstruction and the Thomson diagnostic have radial uncertainties, leading to uncertainties of up to 1.5 cm in some cases [16].

Even though the ion temperature T_i was measured by charge exchange emission spectroscopy, no reliable data was obtained in the very plasma edge where the simulations were conducted. Additionally the particle diffusion and heat diffusion coefficients are plotted with a dotted line in blue. The simulated profiles are within the experimental scatter and reproduce the profile shape of the electron density. No significant difference in upstream profile shape is observable between the 2D and 3D geometrical configurations.

In figure 6 the simulated ion saturation current and plasma temperature at the divertor targets are depicted for both simulation cases. Again, the results of the 3D simulation are depicted by a solid line and the 2D results are represented by a dashed line. Results for the inner target are coloured in red while outer target results are presented in blue. Both the experimental values for the ion saturation current j_{sat} and the plasma temperature at the divertor target $T_{e,target}$ were measured with Langmuir probes, and the experimental data for the heat flux density perpendicular to the outer target $q_\perp$ was measured with an infrared camera. Note that the IR data is shifted by -0.05 MW m^{-2} due to a strong background.

While the simulated profiles agree reasonably well with experimental data for the outer target, experimental results exhibit a much more pronounced asymmetry between inner and outer target for both ion saturation current and plasma temperature with significantly lower values at the inner divertor target. In both simulations, only the heat flux hints at the strong in–out-asymmetry. Due to the higher heat flux densities, the outer divertor is physically more problematic and also has a stronger influence on properties at the outer mid-plane. Matching both the inner and the outer divertor with simulation results at the same time has proven difficult [17, 18], even in simulation schemes that include divertor current and drift

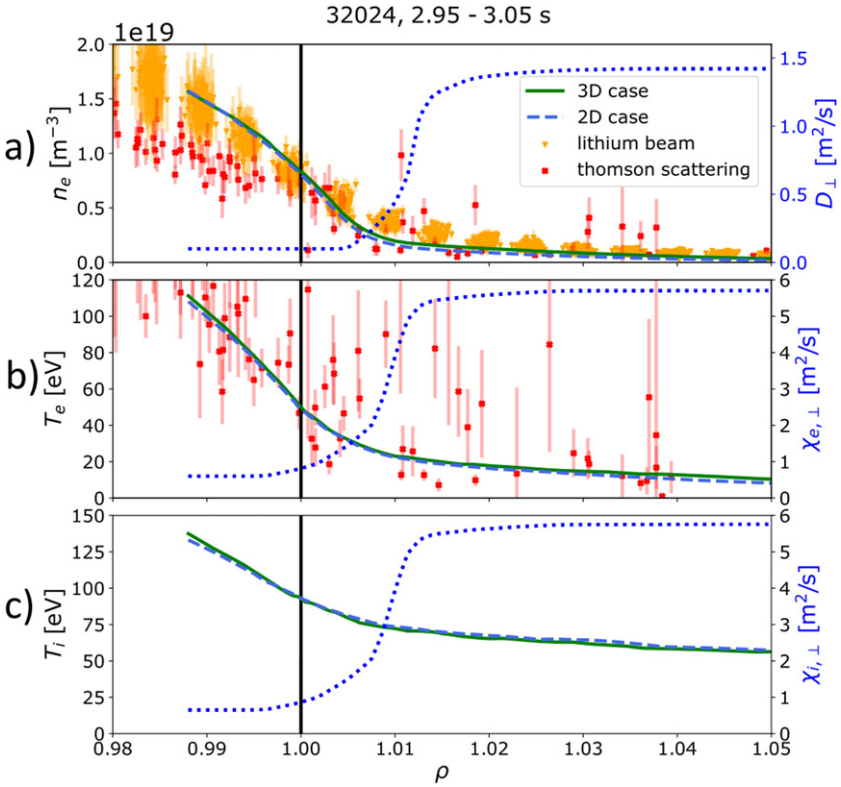

Figure 5. Comparison of 3D and 2D simulation results with experimental data upstream at the outer mid-plane. (*a*) Density: experimental data from Thomson scattering and lithium beam diagnostics. (*b*) Electron temperature: experimental data from Thomson scattering diagnostics. (*c*) Ion temperature.

terms. Since EMC3-EIRENE does not yet include current and drift terms and in this article we are particularly interested in properties at the outer mid-plane, matching the experimental data for the outer divertor is sufficient for our analysis.

3. Influence of geometrical differences on plasma properties

The simulated plasma solutions in 2D and 3D geometry were analysed at several toroidal angles and observed values in poloidal cross-section for n_e, T_e and T_i are very similar: the simulated temperature profiles at the divertor target differ by roughly 3 eV and heat flux densities by up to 0.02 MW m^{-2} between the 2D and the 3D solution.

However, surprisingly large discrepancies in plasma flow patterns, neutral atom and molecular densities as well as ionisation source distributions are observed especially on the LFS where the heat-shield geometry differs.

To highlight that these differences occur not only at toroidal angles where the plasma is locally disturbed by 3D structures, the simulations are compared at $\phi = 24.5°$ in figure 7, far away from the poloidal limiters and the probe at the outer mid-plane. The green lines represent projections of the heat-shield geometry in the poloidal plane.

In figure 7(*a*) the neutral number density is plotted for both cases. In the 2D case a region of higher densities can be seen close to the gap between the main chamber's outer heat-shield and the outer divertor structure (region indicated by the grey rectangle) when compared to the 3D case. This gap corresponds to the outer bypass region indicated in figures 3 and 4. The inner bypass is the gap between main chamber wall and inner divertor structure. In both cases, neutrals can re-enter the plasma via both bypasses after leaving the divertor at the bottom through the pumping gaps and travel upwards behind the divertor heat-shield. On the HFS the neutral number densities exhibit a similar pattern close to the inner bypass in both simulations. In 3D geometry, the region of higher neutral number densities extends further up the outer mid-plane along a reservoir of neutral particles in the far SOL. This is expected because in the 3D case neutrals by passing the outer divertor heat-shield can move further upwards poloidally between the limiters, while their poloidal movement is restricted by the main chamber heat-shield in the 2D case.

Correlating to the neutral distribution, the ionization source distribution in figure 7(*b*) also exhibits stronger sources along the outer mid-plane in the 3D case. The grey rectangle again highlights the area close to the outer bypass and in the enlarged image detail an additional spatial broadening of the ionization source distribution is apparent when compared to the image detail of the 3D case. This corresponds to the higher neutral number densities observed in the same area.

Especially the difference in ionization source distribution has an impact on the plasma flow pattern indicated by the Mach number M in the poloidal cross section in figure 7(*c*). The Mach number is the ratio of plasma velocity v_i to the

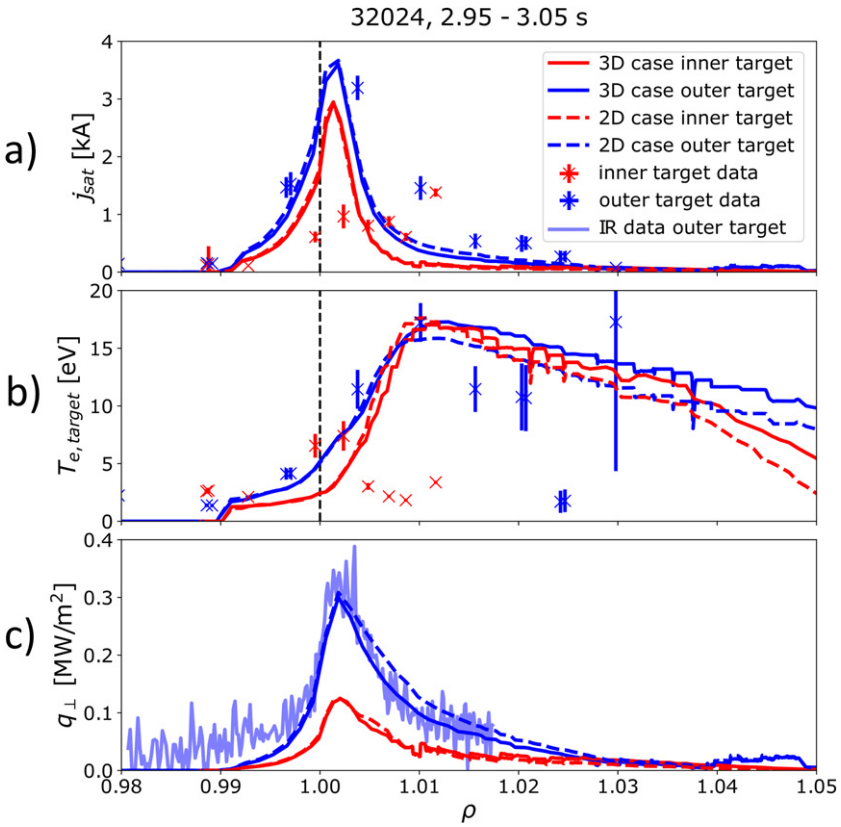

Figure 6. Comparison of both 3D and 2D simulation results with experimental data downstream at the divertor target. (*a*) Ion saturation current: experimental data from Langmuir probes. (*b*) Plasma temperature at the divertor target: experimental data from Langmuir probes. (*c*) Heat flux perpendicular to the divertor target: experimental data from an infrared camera.

speed of sound c_s

$$M = \frac{v_i}{c_s} = \frac{v_i}{\sqrt{\frac{T_e+T_i}{m_i}}}. \tag{3}$$

Positive Mach numbers indicate flow in toroidal direction and eventually towards the inner divertor, while negative Mach numbers indicate flow towards the outer divertor. In figure 7(*c*) the point of flow reversal from outer to inner divertor in the 3D case is located at a much lower poloidal position compared to the 2D case, creating a different plasma flow pattern on the LFS. Furthermore, a pronounced flow in toroidal direction, indicated by the black arrow in the 3D case, shows the impact of the mid-plane collector probe that is located at 42.5°, demonstrating that the simulated plasma flow is influenced even in a distance of 18° in the presented simulations.

The observed differences in neutral number density, ionization source distribution and plasma flow can be attributed to different transport paths for neutral particles in 2D and 3D geometry. In the 2D case neutral particles outside of the first wall structure at the LFS can only enter through the outer bypass at all toroidal angles where they immediately enter the hot edge plasma. It is therefore expected that the neutral number density and also the ionization sources in this poloidal region are high. In the 3D case on the other hand, this poloidal restriction of neutral particle movement is only given at the toroidal angles, where the limiters are located. At other toroidal angles particles can move poloidally upwards without contacting the hot plasma, before their movement is restricted by the inner heat-shield of the 3D geometry. This results in a reservoir of neutral particles between the limiters from where they can enter the plasma at different poloidal positions, reaching locations further upstream above the position of the outer bypass.

The difference in poloidal positions where neutrals can enter the plasma is also reflected in the ionization source distribution which then drives the plasma flow pattern. In figure 8 the ionization sources and neutral number densities were integrated radially and toroidally to identify contributions of different poloidal areas. Both cases show higher neutral number densities around the outer bypass. At higher poloidal indices, the neutral number density in the 2D cases drops quickly, while contributions in the 3D cases are slightly decreasing up to the position of the MEM. A very similar behaviour can be seen in the ionization sources. This decrease in poloidal direction of neutral number density and ionization sources in 3D geometry can be explained by considering the transport paths of the neutrals, that predominantly come from the divertor structure. The small, toroidally symmetric gap in the geometry, that feeds the outer bypass (compare figure 3) behaves like a line source for neutrals that pass through and a barrier for neutrals that do not directly pass through, with the latter leading to a higher amount of neutrals around the outer bypass in both 2D and 3D geometry. In 3D geometry the momentum in poloidal direction

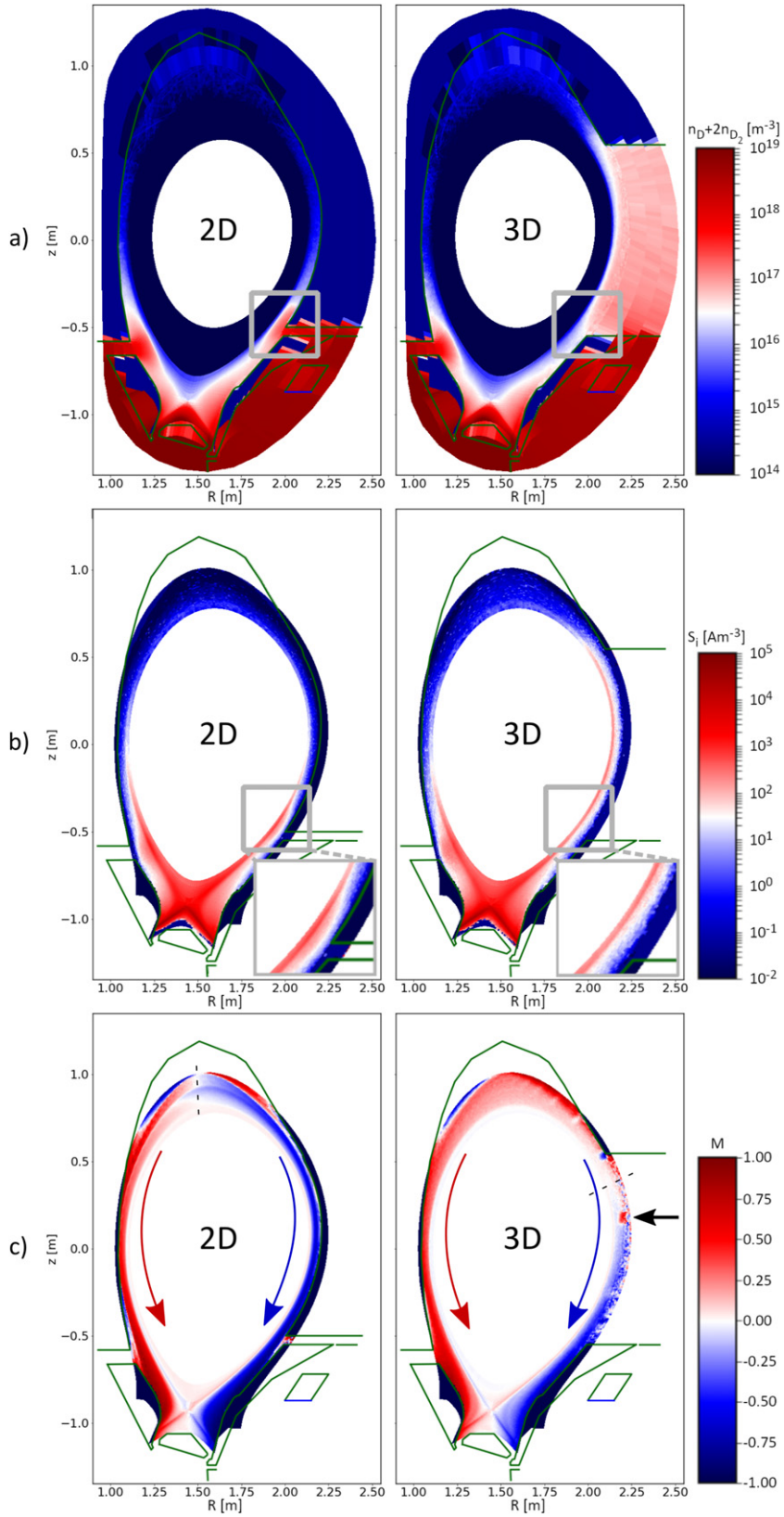

Figure 7. Comparison of data in the poloidal cross sections from the 2D (left) and 3D (right) simulation at $\phi = 24.5°$. (*a*) Distribution of the neutral number density. Indicated by the grey rectangles is the outer bypass region. (*b*) Ionization source distribution. The same region as in (*a*) is indicated by the grey rectangle. (*c*) Plasma flow pattern as indicated by the Mach number. The dashed black line indicates the rough position of flow reversal from outer to inner divertor, while the red and blue arrows indicate the projection of the flow direction in the 2D plane. In the 3D case, the black arrow indicates the flow in toroidal directions towards the MEM.

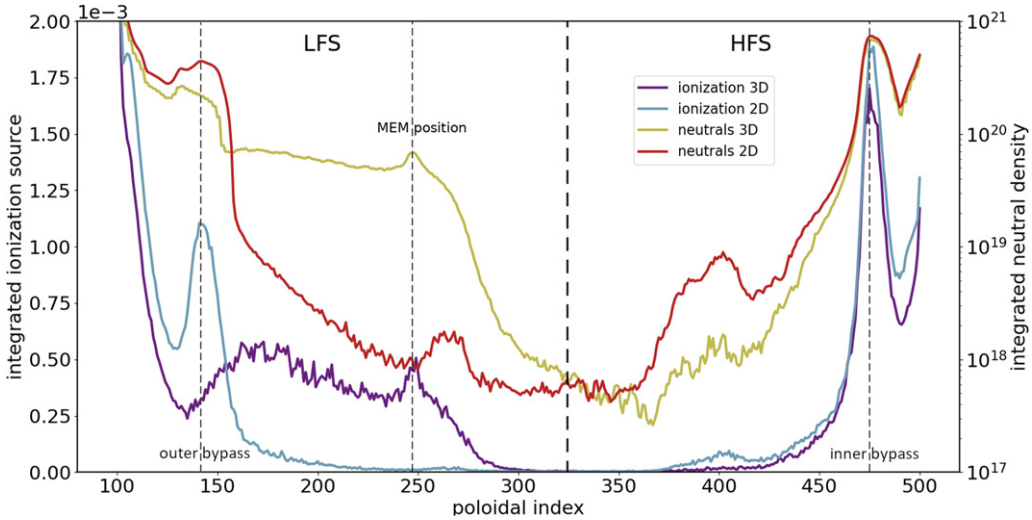

Figure 8. 2D and 3D ionization source and neutral number density (sum of atom and molecular neutral number density) distributions along the poloidal index, integrated over the radial and toroidal indices in the SOL, outside of the divertor, region from 30° to 60°. Note that the ionization is plotted linearly, while the neutral number density is plotted logarithmically.

of neutral particles that passed through the gap moves them poloidally upwards and they do not enter the plasma directly at the outer bypass. The number of particles that enter the plasma at higher poloidal indices then decreases with distance to the gap in the outer bypass. In 2D geometry all particles that pass through the gap are scattered at the LFS heat-shield and can only enter where the outer bypass guides them to the plasma.

Note that the effect of the mid-plane collector probe is clearly visible in neutral number density and ionization sources in the 3D case. This peak consists of particles that were recycled at the mid-plane collector probe and scattered particles from other sources. Another major peak can be seen around the inner bypass. There, neutral number densities in both cases are almost identical and ionization sources only differ slightly. It is clearly visible that differences on the LFS are much more pronounced than on the HFS.

In figure 9 the number of launched particles during the EIRENE part of the EMC3-EIRENE plasma solution iteration is shown for different locations (see also figures 3 and 4 for the indicated areas). The divertor regions 'inner target' and 'outer target' are responsible for the majority of launches from recycling in both geometries. However, in 2D geometry more particles are launched in the LFS region 'outer bypass', while in 3D geometry more particles are launched particularly from the LFS regions 'outer wall 1' and 'outer wall 2', where the rib-limiters are located.

To exclude these differences in recycling sources as the main contributor to the effects observed in neutral number densities, the contribution of different neutral launch locations was investigated: the launches of neutral particles from recycling is restricted to the areas 'inner target' and 'outer target' in the divertor, which are identical in both geometries. All other recycling sources are switched off. In figure 10 the resulting neutral particle distribution was again integrated radially and toroidally and compared to the results with neutral particle sources from recycling at all heat-shield elements (see

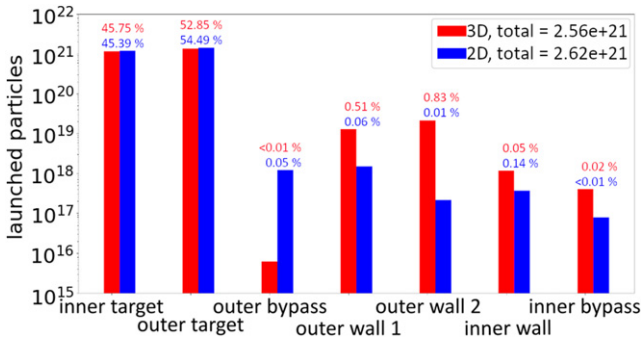

Figure 9. Neutral particles launched from different areas as a result of recycling in 2D and in 3D geometry. The fractions indicate the launched particles of an area divided by the total number of launched neutral particles from recycling. Wall areas are indicated in figures 3 and 4.

in figure 8). The curves with only divertor launches are normalized by their contribution to all launches from recycling sources to enable a quantitative comparison. The reservoir of particles between the limiters is still almost fully pronounced in the 3D case, when recycled particles are only coming from the divertor structure. The small peak at the MEM position can be attributed to scattering of neutrals and is not related to neutrals launched from the MEM. In the 2D case, the missing peak above the MEM position around the poloidal index of 400 can be explained by a leading edge on the LFS heat-shield, that contributes a significant number of neutrals.

Comparing the radially and toroidally integrated ionization source distributions for restricted launched from recycling areas in figure 11 shows even less differences to the non restricted case. In 3D geometry the most notable difference can be seen around the MEM, while on the presented scale the 2D results differ mostly at the HFS wall.

It thus can be concluded that the differences in the neutral number densities and the related differences in ionization

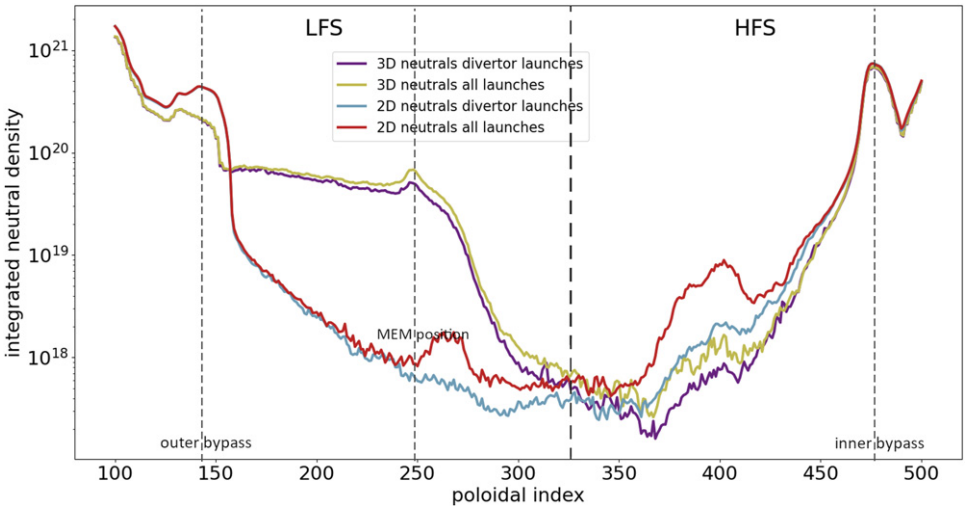

Figure 10. 2D and 3D neutral number density (sum of atom and molecular neutral number density) distribution along the poloidal index, integrated over the radial and toroidal indices in the SOL, outside of the divertor region, from 30° to 60°. Divertor launches and all launches correspond to the same areas as in figure 11.

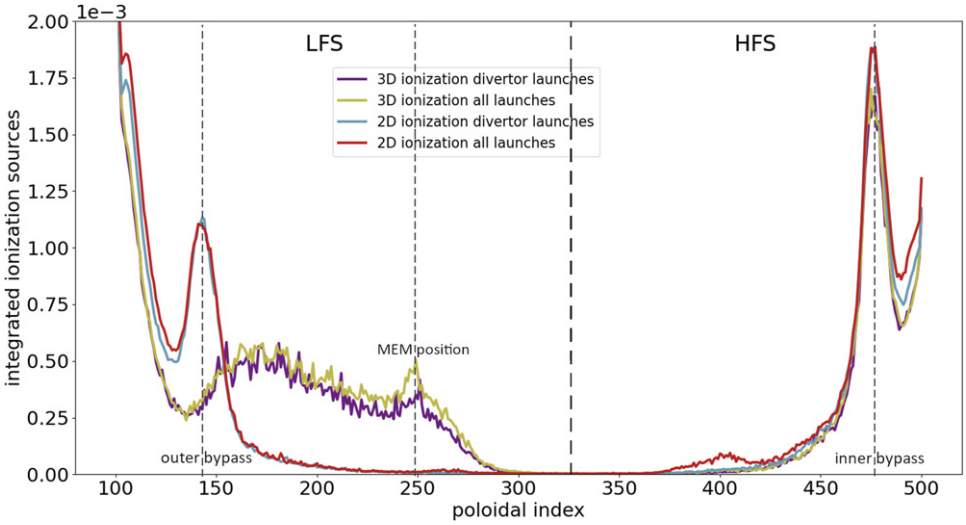

Figure 11. 2D and 3D ionization source distribution along the poloidal index, integrated over the radial and toroidal indices in the SOL from 30° to 60°. All launches indicate that particles from all wall areas (see figures 3 and 4) were launched while divertor launches indicate that only particles from areas inner target and outer target areas were launched.

source distribution and plasma flow are not an effect of different recycling sources at the LFS wall. The differences can rather be explained by different transport paths for the neutrals from the divertor to the main chamber, only available in 3D geometry.

While the differences in the flow patterns apparently do not impact profiles of T_e, T_i or n_e they are expected to have a strong impact on impurity migration and may potentially change the impurity redistribution notably.

In figure 12 a poloidal cross section of the distribution of the N impurity at $\phi = 24.5°$ is indicated by the sum over all charge states, including neutral impurities. In the detailed area around the outer bypass more impurities are present in the 2D case than in the 3D case, which can again be explained by the restriction of poloidal movement in the 2D geometry. Another difference is visible at the top of the main chamber where in the far SOL, the impurity density for every charge state is significantly higher in the 2D case. As the amount of impurities is scaled in order to match the simulated impurity radiation with the experimentally determined radiated power, this can be explained by observed differences in the ion temperature, which similar to the electron temperature (see figures 5(*b*), 6(*b*) and 14), is also slightly larger in the 3D case.

4. Influences on the mid-plane collector probe

One motivation for this work is the discrepancy between model and experiment in the amount of deposited ^{15}N on the MEM found in [4]. A possible explanation for this discrepancy is the way the plasma parameters at the MEM were calculated from the available 2D SOLPS plasma solution in [4], where

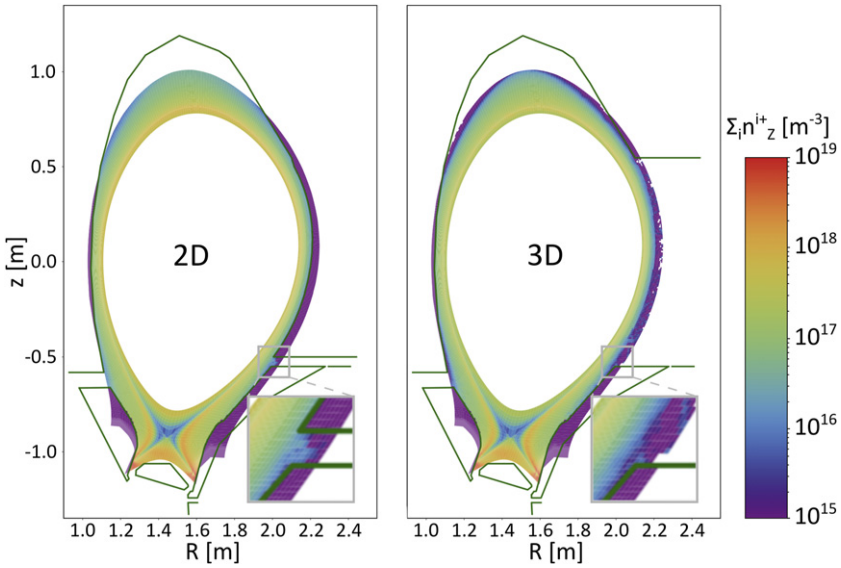

Figure 12. Poloidal cross section at $\phi = 24.5°$ of the sum over all charge states of the N impurity in the 2D (left) and 3D case (right).

the author approximated the flux of impurities following

$$\Gamma_{\mathrm{N}} = n_{\mathrm{N}}\sqrt{\frac{T_{\mathrm{i}}}{2\pi m_{\mathrm{N}}}}, \tag{4}$$

with n_{N} being the density of N^{15} in the plasma cell where the flux is calculated and m_{N} the mass of N^{15}. The so calculated values of Γ_{N} were then fitted with an exponential decay to extrapolate them from the grid edge outward along the MEM. The deposition was estimated by integrating the flux over time and assuming an effective reflection/re-erosion fraction of 0.25. While this is not unreasonable it cannot capture the dynamic interaction of particles from the MEM with other wall elements and vice versa.

In this article we focus on the main plasma parameters along the radial extent of the MEM. We compare values of the plasma flux Γ, as well as T_{e} and T_{i} along the MEM as calculated by EMC3-EIRENE in 2D and 3D geometry. Additionally we use the approximation in equation (4) that was used for Γ_{N} in [4] to compute values for the main ion flux Γ that can be compared to the EMC3-EIRENE results. In the 2D case the fluxes are calculated using equation (14) in [10], to calculate the flux onto the probe as

$$\Gamma_{\mathrm{Hutch}} = n_{\infty}\mathrm{e}^{M_{\infty}-1}c_{\mathrm{s}}, \tag{5}$$

where M_{∞} and n_{∞} are the Mach number and the density of the undisturbed plasma in 2D geometry. To compare the calculated and simulated fluxes to the impurity flux that is used in [4] the main ion flux is also calculated using the same approximation as in equation (4), i.e.:

$$\Gamma_{\mathrm{Meisl}} = n_{\mathrm{e}}\sqrt{\frac{T_{\mathrm{i}}}{2\pi m_{\mathrm{e}}}}. \tag{6}$$

In figure 13 the main ion fluxes and density radially along the MEM are compared for the different approaches.

The main ion flux onto the MEM side facing the distant limiter extracted from the 3D case is up to 2.29 times larger than the flux calculated from the 2D background plasma following equation (5). On the other hand, calculating the flux following equation (6) yields a flux that is about 25% smaller than simulated in 3D geometry.

The fall-off lengths for both calculated fluxes from the 2D case are larger than the fall-off length in the simulated 3D flux. While the simulated 3D flux yields $\lambda_{3\mathrm{D}} = 11.02$ mm the calculated fluxes end up at $\lambda_{2\mathrm{D,Hutch}} = 16.03$ mm following calculations in [10] and $\lambda_{2\mathrm{D,Meisl}} = 12.06$ mm taking equation (6).

Another sensitive parameter for the deposition of impurities are the ion and electron temperatures, as both the sputter and the reflection yields have non-linear dependencies on the particles impact energy, which is assumed to follow

$$E_{\mathrm{impact}} = 3T_{\mathrm{e}} + 2T_{\mathrm{i}}. \tag{7}$$

In figure 14 both electron and ion temperature at the mid-plane-collector probe in 3D geometry are plotted radially together with the electron and ion temperature of the plasma at the same position in 2D geometry. The electron temperatures at the probe tip differ by roughly 1.7 eV and the ion temperatures by about 1.5 eV, which is only about 2.7% for the ion temperatures, but around 17.9% for the electron temperatures. Additionally, the fall-off length for both ion and electron temperature is significantly larger in 2D geometry (48% for the electron temperature and by 142% for the ion temperature) compared to the 3D geometry. In figure 14 the black, dashed line indicates the last data point in 2D geometry. Data points radially further outside in 3D geometry are therefore located in the limiter shadow, where temperatures are expected to drop quickly. Indicated by the red-line is the fall-off for the ion temperature in the limiter shadow with a fall-off length of 10.31 mm, compared to 24.82 mm if only a single exponential is used for fitting. Even if the steep fall-off in the limiter shadow is omitted, the fall-off lengths in 2D geometry remain slightly larger than in 3D geometry.

Overall the absolute values of electron and ion temperatures are similar in 3D and 2D geometry and also the ion flux

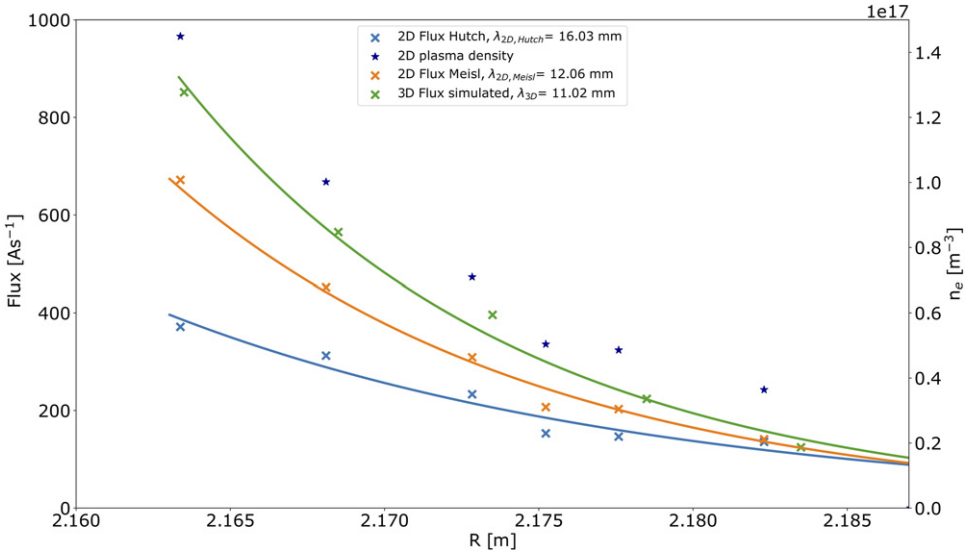

Figure 13. Particle flux towards the side of mid-plane collector probe, that is almost perpendicular to the toroidal magnetic field. The green crosses and line represent the simulated flux in 3D geometry and an exponential fit respectively, while the blue crosses and line shows the calculated flux in the 2D case following [10]. Depicted in orange is the calculated flux assuming equation (6).

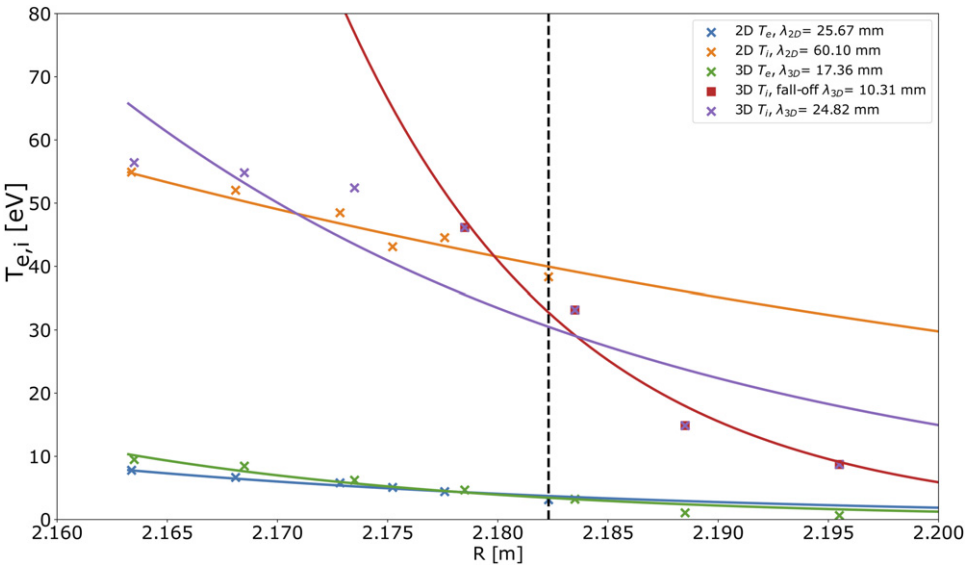

Figure 14. Electron and ion temperature at the side of the mid-plane collector probe facing the distant limiter in 3D geometry (electrons: green, ions: purple) and at the same position in the plasma in 2D geometry (electrons: blue, ions: orange). The lines are exponential fits to determine the fall-off length. The red line indicates the fall-off length of the ion temperature outside a plateau region and the black dashed line marks the outer most data point of the 2D geometry.

calculated with equation (6) in 2D geometry is not significantly different from the fluxes obtained by the 3D simulation. Differences are mainly observed in the fall-off lengths. It must therefore be concluded that the differences between measured N^{15} deposition profiles at the MEM and 2D modelling results in [4] are not an effect of the 3D plasma background parameters, but are related to the effects of 3D geometry on N^{15} migration to and N^{15} recycling at the MEM.

5. Summary and outlook

This paper shows that in tokamak geometry, where usually toroidal symmetry is assumed both in the divertor and the main chamber, geometrical asymmetries at the LFS have notable effects on simulation results, especially when one is interested in neutral particle distributions, ionization sources and the plasma flow pattern. These effects have been shown to

not be local near limiters or probes, but global, impacting the plasma flow patterns even far from the disturbance. The underlying cause has been identified to be a difference in transport paths for the neutrals. In the 3D geometry, neutrals that bypass the divertor structure can travel toroidally to also bypass the limiters and enter the plasma at different poloidal angles than in the 2D case. In the 2D case this movement is limited by the toroidally symmetric LFS heat-shield.

For a mid-plane collector probe, analytically calculated fluxes from the 2D case were compared to simulated fluxes in the 3D case. This shows that the flux values in 2D underestimate the simulated flux by more than a factor of 2 at the probe tip when following the approach in [10] and still by about 25% when the flux is calculated as in [4]. Fall-off lengths are overestimated in both ansatzes with 16.03 mm using the ansatz in [10] and 12.06 mm with the flux calculation as in [4], compared to 11.02 mm as obtain from simulation results in 3D geometry. The radial electron and ion temperature profiles at the mid-plane collector probe only differ slightly between both geometries. The ion temperature at the probe tip in 2D geometry is roughly 1.5 eV smaller and the electron temperature by about 1.7 eV compared to results in 3D geometry. However, observed differences are not sufficient to explain the discrepancies between simulated and measured deposition of N^{15} as reported in [4]. It has to be concluded that observed discrepancies are not an effect of the plasma parameters in 3D geometry, but are related to the effects of 3D geometry on N^{15} transport to and from the mid-plane collector probe. Testing this hypothesis however requires a full 3D WallDYN calculation which is the focus of a future publication currently under preparation.

Acknowledgments

This work has been carried out within the framework of the EUROfusion Consortium and has received funding from the Euratom research and training programme 2014–2018 and 2019–2020 under Grant Agreement No. 633053. The views and opinions expressed herein do not necessarily reflect those of the European Commission.

ORCID iDs

L. Bock https://orcid.org/0000-0001-6714-6424
D. Brida https://orcid.org/0000-0002-8647-7058
M. Faitsch https://orcid.org/0000-0002-9809-7490
T. Lunt https://orcid.org/0000-0002-7386-1456

References

[1] Dekeyser W., Bonnin X., Lisgo S.W., Pitts R.A., Brunner D., Labombard B. and Terry J.L. 2016 SOLPS-ITER modeling of the Alcator C-mod divertor plasma *Plasma Fusion Res.* **11** 1403103

[2] Feng Y., Sardei F., Grigull P., McCormick K., Kisslinger J., Reiter D. and Igitkhanov Y. 2002 Transport in island divertors: physics, 3D modelling and comparison to first experiments on W7-AS∗ *Plasma Phys. Control. Fusion* **44** 611–25

[3] Schneider R., Bonnin X., Borrass K., Coster D.P., Kastelewicz H., Reiter D., Rozhansky V.A. and Braams B.J. 2006 Plasma edge physics with B2-Eirene *Contrib. Plasma Phys.* **46** 3–191

[4] Meisl G. *et al* (ASDEX Upgrade Team) 2017 Nitrogen transport in ASDEX Upgrade: role of surface roughness and transport to the main wall *Nucl. Mater. Energy* **12** 51–9

[5] Fischer R., Fuchs C.J., Kurzan B., Suttrop W. and Wolfrum E. 2010 Integrated data analysis of profile diagnostics at ASDEX Upgrade *Fusion Sci. Technol.* **58** 675–84

[6] Schmid K., Reinelt M. and Krieger K. 2011 An integrated model of impurity migration and wall composition dynamics for tokamaks *J. Nucl. Mater.* **415** S284–8

[7] Meisl G., Schmid K., Krieger K., Oberkofler M. and Lisgo S.W. (JET Contributors) 2016 Simulating the nitrogen migration in Be/W tokamaks with WallDYN *Phys. Scr.* **T167** 014079

[8] Feng Y., Sardei F., Kisslinger J. and Grigull P. 1997 A 3D Monte Carlo code for plasma transport in island divertors *J. Nucl. Mater.* **241–243** 930–4

[9] McCarthy P.J., Martin P. and Schneider W. 1999 *IPP-Report 5/85* Max-Planck-Institut für Plasmaphysik

[10] Hutchinson I.H. 1987 A fluid theory of ion collection by probes in strong magnetic fields with plasma flow *Phys. Fluids* **30** 3777–81

[11] Harting D.M. 2008 3-dimensionale Plasmarandschicht-Simulationen in unvollständig ergodisierten Magnetfeldern *PhD Thesis* Heinrich-Heine-Universität Düsseldorf

[12] Reiter D. 2019 *The EIRENE Code User Manual* (http://www.eirene.de/eirene.pdf)

[13] Schmid K. and Lunt T. 2018 3D global impurity transport modeling with WallDYN and EMC3-Eirene *Nucl. Mater. Energy* **17** 200–5

[14] Sun H.J. *et al* 2017 Study of near SOL decay lengths in ASDEX Upgrade under attached and detached divertor conditions *Plasma Phys. Control. Fusion* **59** 105010

[15] Eich T. and Manz P. (The ASDEX Upgrade team) 2021 The separatrix operational space of ASDEX Upgrade due to interchange-drift-Alfvén turbulence *Nucl. Fusion* **61** 086017

[16] Kurzan B. and Murmann H.D. 2011 Edge and core Thomson scattering systems and their calibration on the ASDEX Upgrade tokamak *Rev. Sci. Instrum.* **82** 103501

[17] Chankin A.V. and Coster D.P. 2009 Comparison of 2D models for the plasma edge with experimental measurements and assessment of deficiencies *J. Nucl. Mater.* **390–391** 319–24

[18] Wischmeier M. *et al* 2009 Current understanding of divertor detachment: experiments and modelling *J. Nucl. Mater.* **390–391** 250–4